THE ASTROPHYSICAL JOURNAL, 434:306–318, 1994 October 10

ON THE FORMATION AND EVOLUTION OF SUPER–ASYMPTOTIC GIANT BRANCH STARS WITH CORES PROCESSED BY CARBON BURNING. I. SPICA TO ANTARES[1]

ENRIQUE GARCÍA-BERRO[2] AND ICKO IBEN, JR.[3]
Received 1994 February 15; accepted 1994 April 22

ABSTRACT

A 10 $M_\odot$ model of Population I composition is evolved from the hydrogen-burning main sequence onto the early "super"–asymptotic giant branch (ESAGB), where hydrogen does not burn, the dominant source of surface luminosity is shell helium burning, and carbon burning in the helium-exhausted core converts all of the initial ^{12}C and ^{22}Ne and some of the ^{16}O in this core into isotopes of oxygen, neon, sodium, magnesium, and other heavy elements. The entire ESAGB phase lasts $\sim 4.6 \times 10^4$ yr, and helium burning is the primary source of surface luminosity for all but ~ 3000 yr. The carbon-burning phase lasts $\sim 2 \times 10^4$ yr. In comparison, the main-sequence phase lasts $\sim 2 \times 10^7$ yr, and the core helium-burning phase lasts $\sim 4 \times 10^6$ yr. At the end of the core carbon-burning phase, dredge-up decreases the mass of the hydrogen-exhausted core from ~ 2.46 $M_\odot$ to ~ 1.315 $M_\odot$. During the dredge-up episode, in addition to products of complete hydrogen burning, products of incomplete helium burning are mixed into the hydrogen-rich convective envelope. At the end of the second dredge-up phase, the model has an electron-degenerate carbon-exhausted core of mass ~ 1.285 $M_\odot$. Between the carbon-exhausted core and the hydrogen-rich convective envelope are three layers which are each of mass ~ 0.01 $M_\odot$ and which contain (1) ^{12}C and ^{16}O at comparable abundances by mass; (2) ^{12}C and ^4He at comparable abundances by mass; and (3) mostly ^4He with some ^{12}C. The abundances by mass of the main constituents of the carbon-exhausted core vary significantly through the core. At the center, abundances by mass are $X(^{16}O) \sim 0.80$, $X(^{20}Ne) \sim 0.11$, $X(^{23}Na) \sim 0.03$, $X(^{24}Mg) \sim 0.0075$, and $X(^{26}Mg) \sim 0.01$, whereas, near the edge of the core, $X(^{16}O) \sim 0.19$, $X(^{20}Ne) \sim 0.50$, $X(^{23}Na) \sim 0.04$, and $X(^{24}Mg) \sim 0.27$. The abundance of ^{23}Na is large enough that, if the mass of the SAGB core can grow to ~ 1.37 $M_\odot$, core collapse into a neutron star will be initiated by electron capture on ^{23}Na rather than on ^{24}Mg.

Subject headings: nuclear reactions, nucleosynthesis, abundances — stars: AGB and post-AGB — stars: evolution — stars: interiors — stars: supergiants

1. INTRODUCTION

Stars which develop electron-degenerate cores made of matter which has experienced complete hydrogen, helium, and carbon burning have received only a small fraction of the attention which has been lavished upon stars which develop electron-degenerate cores made of matter which has experienced complete hydrogen and helium burning, but not carbon burning. Since they form a continuous sequence of bright red giants more luminous than the "red giant branch" (RGB) formed by stars with electron-degenerate helium cores, both types of star with cores in which the dominant elements are heavier than helium have been called "asymptotic giant branch" (AGB) stars. For convenience, we shall here use the term AGB to describe only stars with carbon-oxygen cores and designate stars with more highly evolved cores as "super"-AGB (SAGB) stars, reflecting the fact that the average SAGB star (e.g., possibly Antares) is much brighter than an average AGB star (e.g., Mira).

Depending upon the mass and composition of its main-sequence precursor, the initial mass of the helium-exhausted core of a thermally pulsing AGB star can extend from a minimum of ~ 0.5 $M_\odot$ to a theoretical limit of ~ 1.1 $M_\odot$. The initial mass of the carbon-exhausted core of a thermally pulsing SAGB star can extend from a minimum of ~ 1.1 $M_\odot$ to a theoretical limit of ~ 1.37 $M_\odot$ (Nomoto 1984, 1987).

In AGB stars, long periods of hydrogen burning in a thin shell alternate with shorter periods of helium burning which begin with a thermonuclear runaway. During a helium shell flash, neutron-capture nucleosynthesis produces *s*-process elements in a convective shell which extends almost to the base of the hydrogen-rich envelope. After the convective shell disappears, the freshly synthesized *s*-process elements and freshly synthesized carbon are dredged up into the hydrogen-rich envelope. The existence of carbon stars which are of the appropriate luminosity and which are enriched in *s*-process elements demonstrates the essential correctness of the theoretical picture of AGB interior evolution.

In earlier studies of SAGB stars, the emphasis has been on the formation of carbon-exhausted cores more massive than 1.37 $M_\odot$ and on the exploration of the electron-capture induced collapse of such cores (Miyaji et al. 1980; Nomoto 1984, 1987; Miyaji & Nomoto 1987). In SAGB models which form carbon-exhausted cores of mass less than 1.37 $M_\odot$, hydrogen is reignited (Nomoto 1987) and it is reasonable to suppose that a series of helium shell flashes due to the accumulation of helium from the hydrogen-burning shell will occur, each followed by a dredge-up episode. The expected episodes of alternating helium and hydrogen burning have not yet been explicitly followed.

The characteristics of long period variables (LPVs) in the Magellanic Clouds may be interpreted to suggest that, once

[1] Supported in part by the NSF (US) grant AST 91-13662 and the DGICYT (Spain) grant PB90-0912-CO2.
[2] Departament de Fisica Aplicada, Universitat Politécnica de Catalunya, Jordi Girona Salgado s/n, Modulo B4—Campus Nord, 08034 Barcelona, Spain. garcia@etseccpb.upc.es.
[3] Astronomy and Physics Departments, University of Illinois, 1002 West Green Street, Urbana, IL 61801. icko@sirius.astro.uiuc.edu.

hydrogen is reignited, *s*-process nucleosynthesis in a helium-burning zone and dredge-up occur. Wood, Bessel, & Fox (1983) find that LPVs with larger than normal ZrO line strengths form a sequence in the log L–log P (L = luminosity, P = pulsation period) plane which is an extension to higher luminosities of the log L–log P relationship defined by Mira variables. The fact that isotopes of Zr are formed in the main line of *s*-process nucleosynthesis means that helium shell flashes and dredge-up have occurred. Since *s*-process nucleosynthesis takes place in a carbon-rich environment, it means further that fresh carbon has been dredged up. The fact that the ZrO-rich stars are not carbon stars could mean either that the SAGB phase is aborted before enough carbon has been dredged up to overwhelm oxygen, or that dredged-up carbon is quickly converted into nitrogen at the base of the hydrogen-rich convective envelope, or both. It is probable that both of these possibilities are realized, the first one because the paucity of ZrO-rich LPVs suggests a lifetime of only $\sim 10^5$ yr, and the second one because the ZrO-rich LPVs are also super–Li rich (Smith & Lambert 1989, 1990). The formation of Li is probably a consequence of the fusion of ^{3}He with ^{4}He to form ^{7}Be at the base of the hydrogen-rich convective envelope, followed by transport of ^{7}Be outward to temperatures where electron capture on ^{7}Be to form ^{7}Li is more likely than proton capture with the formation of unstable ^{8}B (Cameron 1955; Cameron & Fowler 1971; Ulrich & Scalo 1972; Sackmann, Smith, & Despain 1974; Smith, Sackmann, & Despain 1973; Scalo, Despain, & Ulrich 1976; Sackmann & Boothroyd 1992; Boothroyd, Sackmann, & Ahern 1993). The final part of the argument is that temperatures high enough for ^{3}He to fuse with ^{4}He are also high enough for ^{12}C and ^{13}C to burn protons and convert dredged-up carbon into nitrogen as rapidly as it is dredged-up (Iben 1975).

This paper constitutes the first in a series, one aim of which is to establish the theoretical justification for this interpretation of the observations. Our investigations, which provide information about the composition achieved after complete carbon burning, also have relevance for the understanding of close binaries which experience the nova phenomenon, and for the understanding of the outcome of mergers of white dwarfs in the dense stellar environment of globular clusters (e.g., Sigurdsson & Hernquist 1992; Chen & Leonard 1993).

It has been established that, in many novae, the abundances of elements heavier than helium in the ejected nova shell is orders of magnitude larger than could have been produced by hydrogen burning in the hydrogen shell flash which powers the outburst (Mustel & Boyarchuk 1959, 1960; Truran 1985, 1990; Williams 1985). This means that matter from the underlying white dwarf has been mixed with matter in the hydrogen-rich accreted envelope prior to or during the outburst (see Fujimoto & Iben 1992 for a recent quantitative estimate). Thus, in order to fully understand the physics of the nova phenomenon, it is necessary to know the abundances in the underlying white dwarf. Several nova outbursts show excesses of neon. Modest excesses (mass fraction less than ~ 0.015) can be understood as due to mixing between accreted matter and matter in the interior of a "CO" white dwarf produced by an AGB precursor. Although the CO white dwarf is composed predominantly of ^{12}C and ^{16}O, most of the CNO elements in the main-sequence precursor of the AGB star have been converted into ^{22}Ne in the convective shell formed during a helium shell flash; for a Population I initial composition, the abundance by mass of ^{22}Ne near the surface of the underlying white dwarf is ~ 0.01–0.02. On the other hand, there are several instances in which the abundance by mass of neon appears to be far in excess of 0.015, nova V1370 Aql (1982) being an example (Snijders et al. 1987). In such cases, it is probable that matter from a white dwarf produced from an SAGB precursor is involved and, in order to make quantitative statements about the extent of mixing between matter in the white dwarf interior and accreted matter, it is important to know the abundances of ^{20}Ne and of other heavy elements after carbon burning has been completed. Dominguez, Tornambè, & Isern (1993) have made progress in this direction, and further exploration is worthwhile.

In this paper, we trace the evolution of a constant-mass model of mass 10 $M_\odot$ and of Population I composition from the main sequence to the cessation of shell hydrogen burning (§ 2), follow the progress of carbon burning until carbon is exhausted at the center (§ 3), and follow subsequent carbon- and helium-burning episodes until carbon is exhausted over the central 1.285 $M_\odot$ of the model and dredge-up has reduced the mass of the hydrogen-exhausted core to 1.315 $M_\odot$. In our next paper, we follow to completion the reduction in the mass of the hydrogen-exhausted core, and follow the subsequent development of the alternating hydrogen-, helium-, and carbon-burning phase which is an extension of the alternating helium- and hydrogen-burning phase experienced by AGB models. Additional papers will (1) explore these same events in constant-mass models of different initial masses, and (2) follow the carbon-burning phase in models which lose most of their hydrogen-rich envelopes in case B and early case C Roche-lobe overflow events.

2. EVOLUTION TO THE CESSATION OF HYDROGEN BURNING

Our initial model is of mass 10 $M_\odot$, and the abundances by mass of ^{1}H, ^{3}He, ^{4}He, ^{12}C, ^{14}N, and ^{16}O are, respectively, $X(^1\mathrm{H}) = 0.706$, $X(^3\mathrm{He}) = 4.11 \times 10^{-6}$, $X(^4\mathrm{He}) = 0.282$, $X(^{12}\mathrm{C}) = 0.00284$, $X(^{14}\mathrm{N}) = 0.00093$, and $X(^{16}\mathrm{O}) = 0.00847$. All other elements are assumed to be initially absent. The opacity parameter in the analytic approximation to the opacity (Iben 1975 and corrections in, e.g., Iben 1993) is chosen as $Z = 0.02$. The equation of state in interior regions is given in Appendix A2 of Iben, Fujimoto, & MacDonald (1992). In regions in which hydrogen or helium burning is taking place, the nuclear-reaction network is the same as that used for many years (e.g., Iben 1965a, b).

The evolutionary track of our model in the Hertzsprung-Russell diagram is given in Figure 1. The time to evolve to a labeled point from the previous point is indicated in the table. Other quantities in Table 1 are stellar radius R (in solar units), central density ρ_c (in g s^{-1}), central temperature T_c (in K), the mass M_{He} of the hydrogen-exhausted core, and the mass M_{CO} of the helium-exhausted core (masses in solar units).

Also shown in Figure 1 are the approximate positions of four stars in the Bright Star Catalogue (Hoffleit & Jaschele 1982). The two components of Spica have masses ~ 7 $M_\odot$ and ~ 11 $M_\odot$ and thus bracket the mass of our model. The fact that the assigned surface temperatures of these two stars are smaller than the surface temperature of the 10 $M_\odot$ model during the main-sequence phase is probably mainly due to the fact that envelope opacities of population I stars are larger than those we have adopted (Rogers & Iglesias 1992; Stothers & Chin 1992). Betelgeuse and Antares are probably more massive than our model and may be in the first, red giant phase of core helium burning. Since the lifetime of this phase for massive

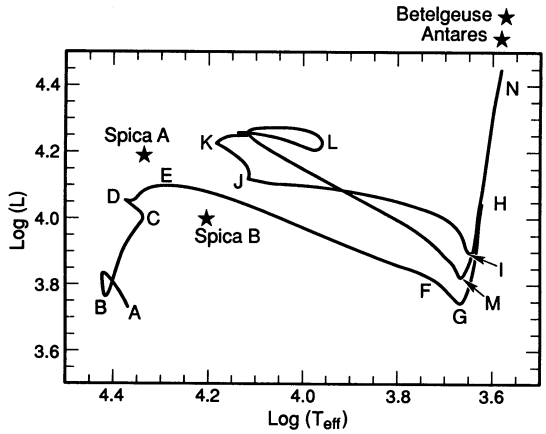

FIG. 1.—The evolutionary track in the Hertzsprung-Russell diagram of a model of mass 10 $M_\odot$ and Population I composition. Times to evolve to each labeled point along the track are given in the second column of Table 1. For comparison, the approximate positions of four stars from the bright star catalog (Spica A and B, Antares, and Betelgeuse) are shown.

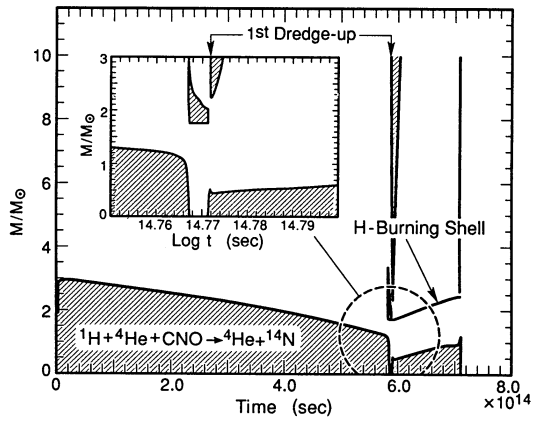

FIG. 2.—Convective regions as a function of time up to the onset of carbon burning. The insert shows with higher resolution the behavior near the end of core hydrogen burning and near the beginning of core helium burning.

stars can be comparable to or larger than the lifetime of the AGB phase for lighter stars, it is perhaps at least as likely that Antares and Betelgeuse are core helium-burning stars as they are AGB stars. In our 10 $M_\odot$ model, the red giant phase of core helium burning lasts $\sim 3 \times 10^5$ yr, and the AGB phase prior to the reignition of hydrogen (the early-SAGB or ESAGB stage) lasts $\sim 5 \times 10^4$ yr. The subsequent thermally pulsing AGB (TPAGB) phase could possibly last as long as 10^5 yr. Since the lifetime of the red giant core helium-burning phase decreases with increasing initial mass, it is not totally excluded that Antares is an SAGB star; in any case, invocation of its lovely name provides motivation and inspiration.

The main-sequence and core helium-burning phases of evolution have been so well documented that it is unnecessary to describe them in any detail. Nevertheless, for completeness, we exhibit in Figure 2 the dependence on time of convective zones and in Figure 3 the dependence on time of radius during these phases. The initial central convective zone in Figure 2 is due to the high fluxes engendered by CN-cycle reactions and persists until hydrogen vanishes at the center. An off-center convective zone forms at $t \sim 5.85 \times 10^{14}$ s ($= 1.85 \times 10^7$ yr) and persists for $\sim 1.6 \times 10^5$ yr. It is due to the release of gravitational potential energy during the overall contraction phase (point C–D in Fig. 1) following the exhaustion of hydrogen at the center. As the model evolves toward the giant branch, a convective envelope forms. Beginning at time $\sim 5.90 \times 10^{14}$ s ($= 1.87 \times 10^7$ yr), the base of the convective envelope extends inward into mass into the region where ^{12}C has been converted into ^{14}N and some ^1H has been converted into ^3He and ^4He; the freshly made isotopes are "dredged-up" to the surface (Iben 1964; Iben & Renzini 1983). At the end of this first dredge-up episode, the surface composition has become $X(^1H) = 0.681$, $X(^3He) = 1.23 \times 10^{-5}$, $X(^4He) = 0.305$, $X(^{12}C) = 0.00179$, $X(^{14}N) = 0.00283$, and $X(^{16}O) = 0.00771$.

During the main-sequence phase, ^{13}C is built up in a narrow region about one-half of the way (in mass) between stellar center and surface. As the first dredge-up episode progresses, the fresh ^{13}C is spread out over the convective envelope, and the surface ratio of ^{12}C to ^{13}C is reduced from an initial value comparable to that found in the interstellar medium to something substantially less than this. For example, in a 5 $M_\odot$ model, the total amount of freshly produced ^{13}C is $\frac{1}{27}$th of the mass of ^{12}C remaining (Iben 1966). If the initial ratio of ^{12}C to ^{13}C is $\sim$40–70 (Hawkins, Craig, & Meyer 1993), dredge-up reduces the ratio to $\sim$16–19. Although we have not calculated it explicitly, a similar reduction will occur in the 10 $M_\odot$ model.

The core helium-burning phase lasts for 3.7×10^6 yr, 2.7×10^5 yr of which is spent as a red giant star (points H–I in

TABLE 1

CHARACTERISTICS OF MODELS AT VARIOUS POINTS IN THE H-R DIAGRAM OF FIGURE 1

Model	$t(10^{14}$ s)	log L	log T_e	log R	log ρ_c	log T_c	M_{He}	M_{CO}
A	0.0000	3.73	4.37	0.65	0.77	7.43	0.000	0.000
B.....	0.1658	3.77	4.41	0.58	0.97	7.50	0.000	0.000
C	5.7468	4.01	4.34	0.85	1.18	7.60	1.702	0.000
D	5.8499	4.05	4.37	0.81	1.79	7.67	1.736	0.000
E.....	5.8807	4.10	4.28	1.02	2.92	7.82	1.742	0.000
F.....	5.9107	3.81	3.72	1.98	3.61	8.16	1.743	0.000
G	5.9117	3.75	3.67	2.06	3.59	8.16	1.743	0.000
H	5.9393	4.00	3.63	2.27	3.54	8.16	1.743	0.000
I	6.0241	3.90	3.65	2.17	3.51	8.18	1.743	0.000
J	6.1210	4.12	4.12	1.36	3.49	8.18	1.800	0.000
K	6.6971	4.23	4.18	1.27	3.46	8.25	2.122	0.000
L.....	7.0679	4.22	3.96	1.71	4.09	8.44	2.415	1.089
M.....	7.0977	3.83	3.67	2.10	5.29	8.61	2.415	1.192
N	7.1055	4.37	3.59	2.53	6.18	8.71	2.415	1.220

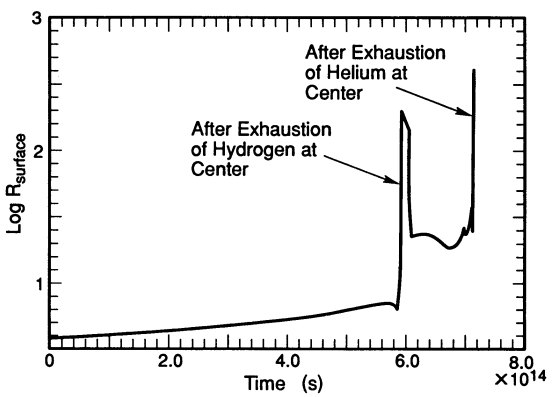

FIG. 3.—Surface radius as a function of time up to the onset of carbon burning.

Fig. 1), and 3.4×10^6 yr of which is spent evolving blueward of the giant branch (points I–M in Fig. 1). At its maximum extent, the convective core has a mass $\sim 1.15\ M_\odot$. At the end of the core helium-burning phase, helium has been exhausted over this mass and hydrogen-burning has increased the mass of the hydrogen-exhausted core from $\sim 1.7\ M_\odot$ to $\sim 2.4\ M_\odot$.

At time $t = 7.0651 \times 10^{14}$ s ($= 2.236 \times 10^7$ yr), helium burning goes to completion almost simultaneously over the inner $\sim 1.1\ M_\odot$ of the model, and helium burning continues in a shell. The helium-exhausted core contracts and heats and, at the same time, essentially all of the matter between a position slightly above the helium-burning shell and the surface expands outwards and cools. Thanks to an increasing opacity in the cooling region, convection again appears in the envelope, and the base of the convective envelope grows inward in mass from the surface. In models of somewhat smaller mass which develop an electron-degenerate core during this episode, the base of the convective envelope extends inward further than it does during the first dredge-up episode; hydrogen ceases to burn, the base of the convective envelope extends inward past the hydrogen-helium discontinuity, and products of complete hydrogen burning are incorporated into the convective envelope (Iben 1966).

In our model, hydrogen burning also ceases, but the onset of carbon burning in the core stalls the inward penetration of envelope convection at a point just above the hydrogen-helium "discontinuity" (where the steepest portions of the ^{1}H- and ^{4}He-abundance profiles are located), and the surface abundances are essentially the same as they were at the end of the first dredge-up episode. Abundances by mass throughout the model when carbon-burning reactions are first introduced (time $t = 7.106 \times 10^{14}$ s $= 2.249 \times 10^7$ yr) are shown in Figure 4. Note that, below the base of the convective envelope located at the mass point $\sim 2.53\ M_\odot$, there is a layer of thickness $\sim 1\ M_\odot$ in which the abundances of ^{4}He and of ^{14}N are substantially larger than at the surface. A rapid inward progress of the base of the convective envelope is resumed when carbon has been exhausted over the inner $1.28\ M_\odot$ of the hydrogen-exhausted core (§ 4). The inward progress continues until the entire ^{4}He- and ^{14}N-rich layer, as well as some matter which has experienced partial helium burning, is mixed into the convective envelope, resulting in a further enrichment of ^{4}He and ^{14}N at the surface.

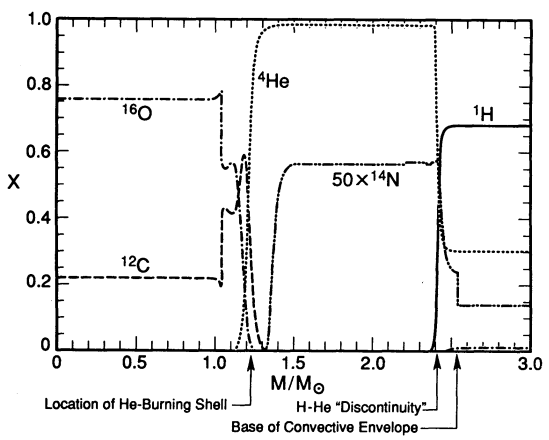

FIG. 4.—Abundances by mass of the main constituents in the model at a time ($\Delta t = 0$), shortly before the inward advance of the base of the convective envelope is stalled by the onset of carbon burning.

3. FROM THE ONSET OF CARBON BURNING TO THE EXHAUSTION OF CARBON AT THE CENTER

In regions within which complete hydrogen and complete helium burning have taken place, we consider reactions between ^{12}C nuclei and between ^{12}C and ^{16}O nuclei, using the cross sections and branching ratios given by Caughlan & Fowler (1988); all reactions involving protons, neutrons, and alpha particles which connect the isotopes shown in Figure 5 are taken into account using cross sections given by Caughlan & Fowler (1988) for charged particle reactions and given by Bao & Käppeler (1987) for neutron-capture reactions. Arrows in Figure 5 mark the reaction channels most frequency followed. We have arbitrarily terminated the reaction network at ^{26}Mg.

In Figure 6 are shown the variations with time of the surface luminosity $L_{\rm Surface}$, the helium-burning luminosity $L_{\rm Helium}$, the carbon-burning luminosity $L_{\rm Carbon}$, the absolute value of the neutrino luminosity $L_{\rm Weak}$, and the rate of "gravitational energy" release $L_{\rm Grav}$. This last luminosity is the integral of $-TdS/dt = -dU/dt - Pd(1/\rho)/dt$, where U is the internal energy per gram and $-Pd(1/\rho)/dt$ is the rate per gram at which work is done *by* the matter (if it is positive) or *on* the matter (if it is negative). $L_{\rm Weak}$ does not include the energy from the beta decays which are part of the carbon-burning network; this energy is included in $L_{\rm Carbon}$. In Figure 6, time is measured from the moment when the carbon-burning network is first invoked (7.106×10^{14} s after the start of the main-sequence phase). Here and in the remainder of this paper, all times are measured from this moment and described in the text as Δt (but still described as t along relevant figure axes in Fig. 17 and beyond). The composition profiles in Figure 4 are for $\Delta t = 0$. In Figure 7 is shown the time development of the central density, the central temperature, and the surface radius.

During most of the time shown in Figures 6 and 7, neutrino losses, which come primarily from the inner half of the core, are relatively closely balanced by the release of gravitational potential energy there. Gravitational potential energy released just below the helium-burning shell almost exactly balances the

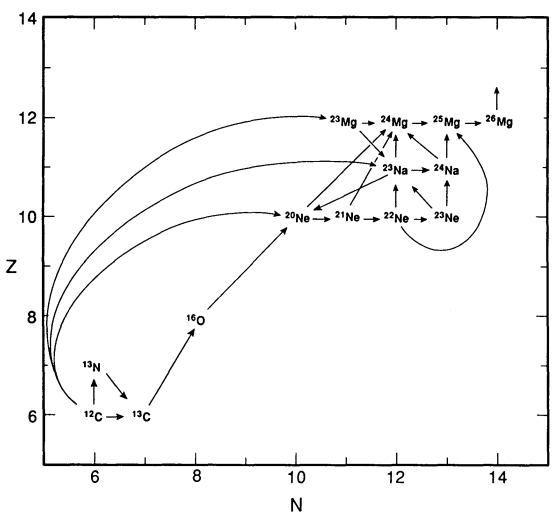

FIG. 5.—Isotopes which are followed explicitly in carbon-burning regions. The ^{12}C-^{12}C and ^{12}C-^{16}O reactions and all neutron-, proton-, and alpha-capture reactions connecting the isotopes shown are taken into account, as are relevant β-decay reactions.

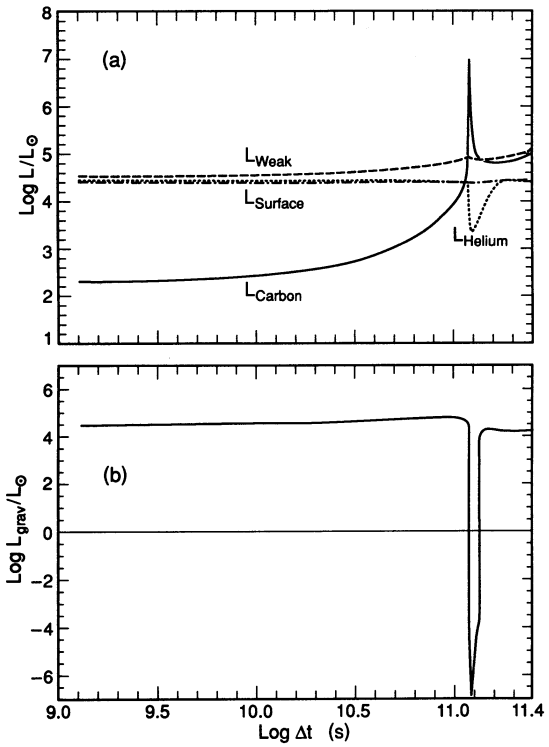

FIG. 6.—The time evolution of surface luminosity $L_{\rm Surface}$, helium-burning luminosity $L_{\rm Helium}$, carbon-burning luminosity $L_{\rm Carbon}$, and the neutrino luminosity $L_{\rm neutrino} = L_{\rm Weak}$ during the beginning of the core carbon-burning phase are shown in (*a*). The rate of "gravitational" energy generation ($L_{\rm Grav}$) is shown in (*b*) Time Δt is measured from the moment when the carbon-burning reaction network is first used (at time $t = 7.105522688 \times 10^{14}$ s $\sim 2.25 \times 10^7$ yr from the start of the main-sequence phase).

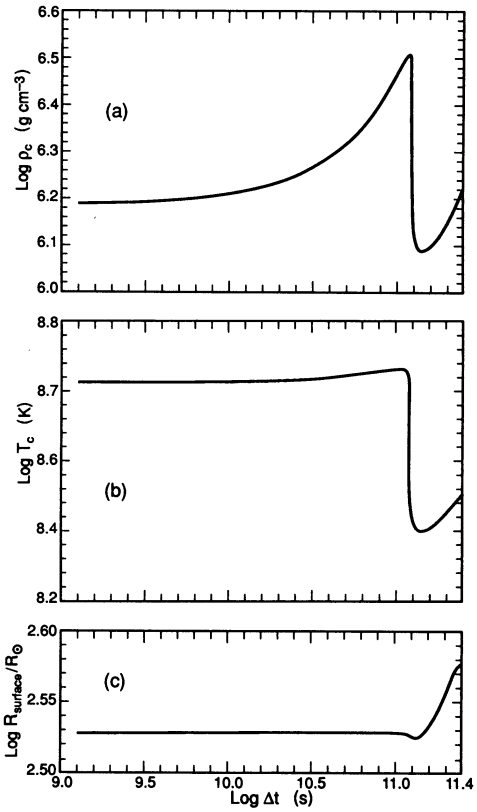

FIG. 7.—Time evolution of (*a*) the central density (*b*) the central temperature, and (*c*) the surface radius. Time is normalized as in Fig. 6.

rate at which work is being done in expanding matter in the region between the helium-burning shell and the base of the convective envelope by energy absorbed from the ambient energy flow. Because of these internal balances, the surface luminosity is essentially equal to the helium-burning luminosity.

However, the injection of energy by carbon-burning reactions, even when the injection rate is relatively modest, alters the response of the rest of the model relative to that which would occur in the absence of this injection. In particular, as we have already noted, the inward penetration of envelope convection stalls. Figures 8–10 describe some properties of a model near the beginning of the stalling phase. The time is $\Delta t = 1.0899913 \times 10^{11}$ s, and the carbon-burning luminosity is approximately 80% of the helium-burning luminosity (Fig. 6*a*).

Energy-generation and -loss rates are shown in Figure 8, luminosity and velocity are shown in Figure 9, and rates of temperature and density change are shown in Figure 10. In Figures 9 and 10, the location of the center of the helium-burning shell is defined as the point where the rate of energy generation by helium burning is at a maximum, and the center of the helium profile is defined as the point where the abundance of helium is at half-maximum. The hydrogen-helium discontinuity is defined as the point where the abundance of hydrogen is at half-maximum. The base of the convective envelope and the place where the carbon-burning rate is at a maximum are also marked.

From Figure 9 it is evident that, over the inner 0.5 $M_\odot$ (log $M/M_\odot < -0.30$), there is essentially an exact global balance between the different energy-generation and energy-loss mechanisms, and, beyond this point, carbon burning contributes only a small amount to the outward flow of energy. Nevertheless, the injection of carbon-burning energy has an influence on the motion of matter throughout the model. Figures 9*b* and 10*b* show that, even though matter in the radiative region between the outer edge of the helium-burning shell and the base of the convective envelope is expanding and moving outward, as is the normal case above a helium-burning shell of an EAGB model, matter throughout the convective envelope is contracting and moving inward, exactly the reverse of the situation prior to the ignition of carbon. From the profile of the rate of increase of temperature (Fig. 10*a*), as well as from the profiles of $\epsilon_{\rm grav}$ (Fig. 8*b*) and of $\epsilon_{\rm Carbon}$ (Fig. 8*a*), it is clear that most of the energy from carbon burning goes into heat and does not contribute to the outward flow energy. However, the deposited heat translates into pressure which modifies the rate at which the core contracts and ultimately affects the motion of matter far beyond the carbon-burning region.

The model which we have just described is in the process of experiencing a carbon-burning "runaway" (see Fig. 6*a*). The carbon-burning luminosity $L_{\rm Carbon}$ increases exponentially until it achieves a maximum value of $\sim 10^7\ L_\odot$. The nuclear energy which is injected is converted into heat in the core, as is evident from the rate of increase in temperature in the carbon-burning region (Fig. 10*a*). The expansion of the core extends to the helium-burning shell and the helium-burning luminosity $L_{\rm Helium}$ declines precipitously. During the relaxation phase following the carbon-burning runaway, contraction and heating allow $L_{\rm Helium}$ to gradually return to the value it had prior to the

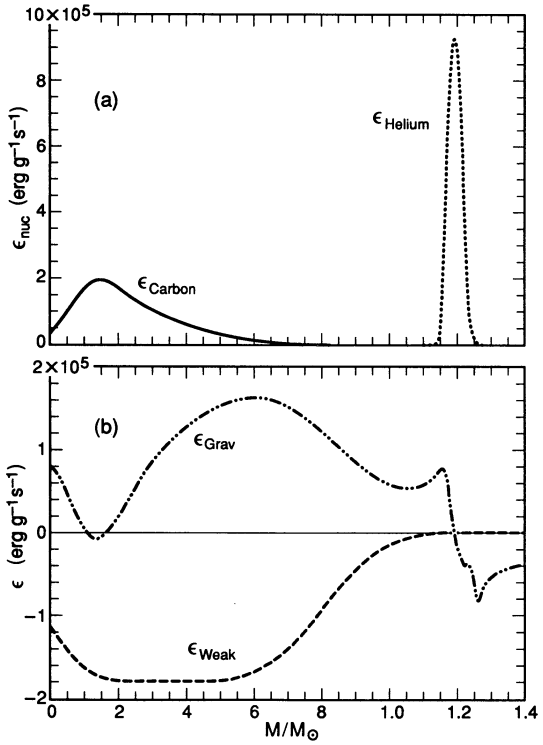

FIG. 8.—Mass dependence of energy-generation and -loss characteristics at time $\Delta t = 1.08999 \times 10^{11}$ s (log $\Delta t = 11.0374$). The rate of energy generation by carbon-burning reactions $\epsilon_{\rm Carbon}$ and by helium-burning reactions $\epsilon_{\rm Helium}$ are shown in the upper panel (*a*), and the rates of gravitational energy release $\epsilon_{\rm grav}$ and neutrino losses (other than by beta decays in the carbon-burning network) $\epsilon_{\rm Weak}$ are shown in the lower panel (*b*).

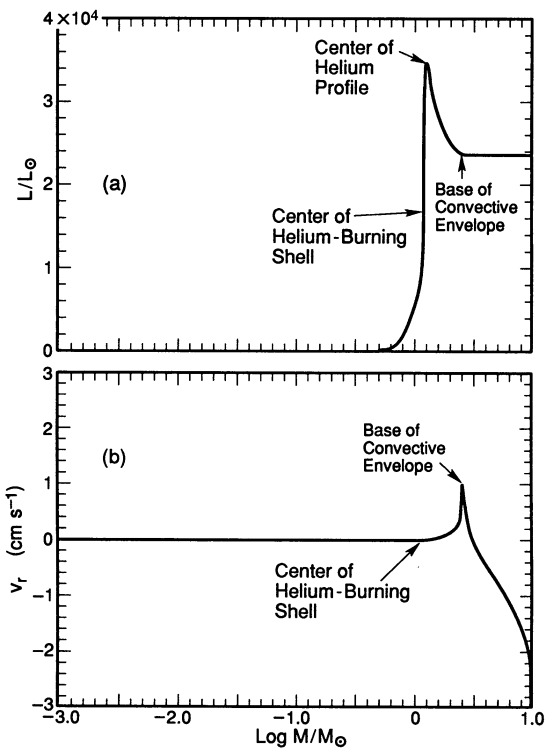

FIG. 9.—Mass dependence of (*a*) the luminosity and (*b*) matter velocity in the same model described in Fig. 8.

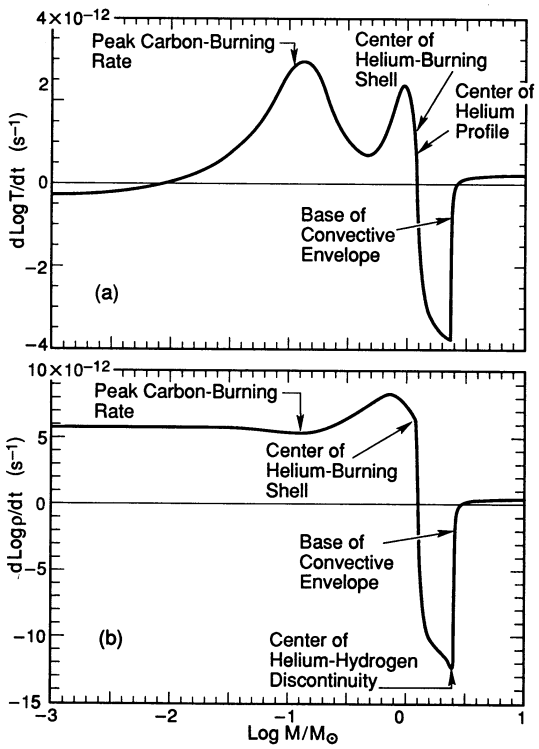

FIG. 10.—Mass dependence (*a*) of the rate of temperature increase and (*b*) of the rate of density increase in the same model described in Fig. 8.

onset of the carbon flash (Fig. 6*a*). As $L_{\rm Helium}$ decreases, the surface radius drops; then, as $L_{\rm Helium}$ increases, the surface radius increases to a new relative maximum (at log $\Delta t \sim 11.4$).

The flux due to carbon burning leads to the formation of convective zones, the time dependences of which are displayed in Figure 11*c*. There are three main convective phases: (1) one during which carbon is depleted over approximately half of the helium-exhausted core in a convective shell that does not grow (in mass) toward the center and does not grow outward (in mass); (2) a second one during which carbon is depleted within two successive convective zones which grow inward in mass until the second eventually reaches the center; and (3) a final phase during which carbon is depleted in a convective shell which evolves toward the surface of the helium-exhausted core. The time-dependent behavior of these phases can be correlated with the time-dependent behavior of $L_{\rm Carbon}$, as shown in Figure 13*a* where the time dependences of other luminosities are shown as well. The first and third convective phases are initiated by strong carbon flashes, and then sustained through extended periods during which $L_{\rm Carbon}$ remains high.

The energy-generation characteristics of a model at a time near the beginning of the existence of the first convective zone is shown in Figure 12. The time is $\Delta t = 1.2271 \times 10^{11}$ s (log $\Delta t = 11.0889$) and the mass in the convective shell is near its maximum value. In Figures 12*a* and 12*b*, we see that the nuclear energy which is emitted in a sharp spike near the base of the convective shell is absorbed throughout this shell in consequence of the work done in expanding matter. From the structure of the $\epsilon_{\rm Grav}$ curve in Figure 12*b*, it is clear that energy is also being absorbed in a narrow radiative region below the base of the convective envelope. The balance between emitted nuclear energy and absorbed energy is illustrated in a different

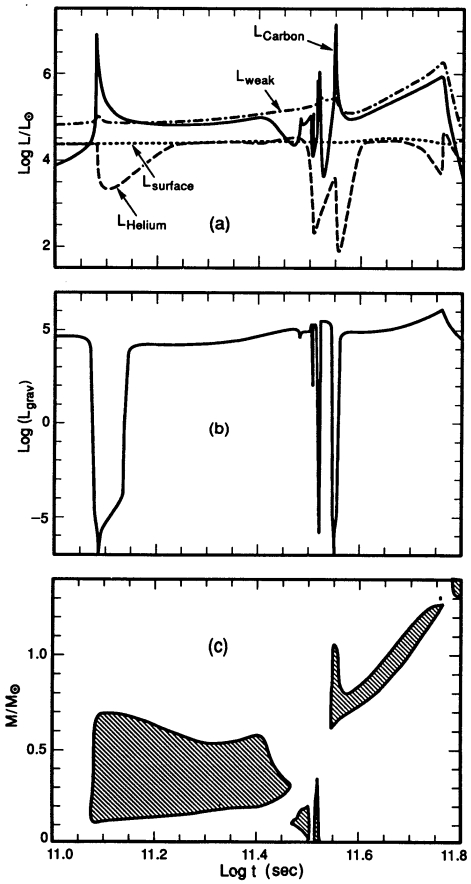

FIG. 11.—Time dependence of (*a*) $L_{\rm Helium}$, $L_{\rm Carbon}$, $L_{\rm Weak}$, and $L_{\rm Surface}$; (*b*) $L_{\rm grav}$; and (*c*) mass boundaries of convective zones. The logarithm of $|L_{\rm grav}|$ is plotted as a negative number if $L_{\rm grav} < 0$.

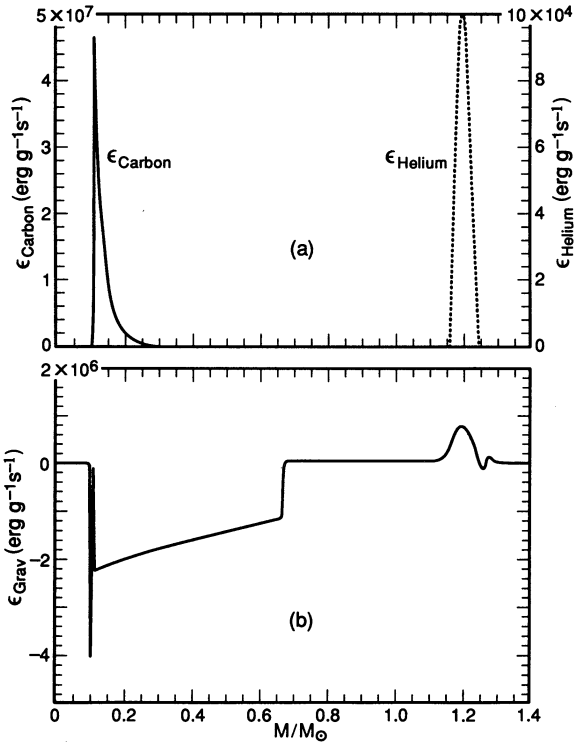

FIG. 12.—Mass dependence (*a*) of $\epsilon_{\rm Carbon}$ and (*b*) of $\epsilon_{\rm grav}$ in a model at time $\Delta t = 1.2270869 \times 10^{11}$ s (log $\Delta t = 11.0889$), when the mass of the convective shell is at a maximum during the first carbon shell flash.

way in Figure 13, which gives luminosity as a function of the mass coordinate. The physical processes which are responsible for different slopes along the luminosity curve are indicated (recall that $\epsilon = dL/dM$).

Abundances by number of isotopes in the hydrogen-exhausted core are shown in Figure 14. The *average* rates (in units of g^{-1} s^{-1}) at which reactions occur within the convective shell are described in Figure 15; each geometric symbol gives the rate of the associated transition according to the algorithm: the number enclosed by the symbol times the rate assigned to the symbol in the key in the lower right-hand corner of the figure. The main channels for the production and absorption of protons, neutrons, and alpha particles are as follows: (1) protons are produced by the $^{12}C + {}^{12}C \rightarrow {}^{23}Na + p$ reaction and absorbed by the $^{12}C(p, \gamma)^{13}N$ and the $^{23}Na(p, \alpha)^{20}Ne$ reactions; (2) neutrons are produced by the $^{13}C(\alpha, n)^{16}O$ reaction and, to a much smaller extent, by the $^{12}C + {}^{12}C \rightarrow {}^{23}Mg + n$ reaction, and are absorbed in (n, γ) reactions in roughly similar proportions by isotopes of C, Ne, Na, and Mg; (3) alpha particles are produced by the $^{12}C + {}^{12}C \rightarrow {}^{20}Ne + \alpha$ and $^{23}Na(p, \alpha)^{20}Ne$ reactions, and are absorbed by the $^{12}C(\alpha, n)^{16}O$ and $^{16}O(\alpha, \gamma)^{20}Ne$ reactions.

Several isotopes that are at trace abundances play an extremely important role in the nucleosynthesis of isotopes that have substantial abundances, demonstrating that the isotopes to include in a nuclear-burning network must not be limited to those which are expected to have a large abundance in the final burning product. Good examples, in addition to the obvious ones (α's, p's, and n's), are ^{13}C and ^{13}N, which are at number abundances of 2×10^{-6} A_0 g^{-1} and 8×10^{-13} A_0 g^{-1}, respectively (A_0 is Avogadro's number, 6.023×10^{23}). These isotopes are primarily responsible for the production of ^{16}O. Another example is ^{24}Na which is at a number abundance of 10^{-9} but makes a major contribution to the production of ^{24}Mg. An important omission from the network is ^{27}Al, as the reaction $^{26}Mg(p, \gamma)^{27}Al$, if it were permitted to occur, would absorb about 10% of the protons produced by the reaction $^{12}C + {}^{12}C \rightarrow {}^{23}Na + p$.

The rate at which carbon-burning reactions inject energy reaches a maximum at about the same time that the mass of the convective shell achieves its maximum value. Profiles of

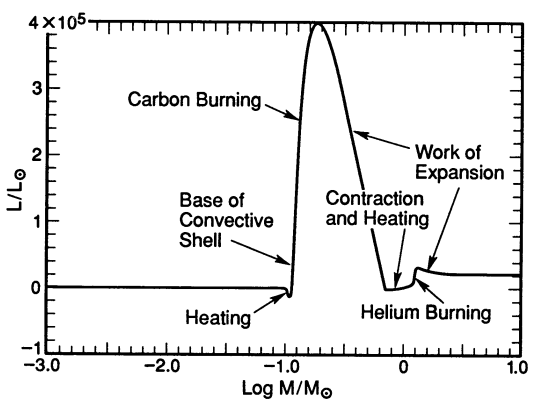

FIG. 13.—Luminosity as a function of mass in the same model described in Fig. 12.

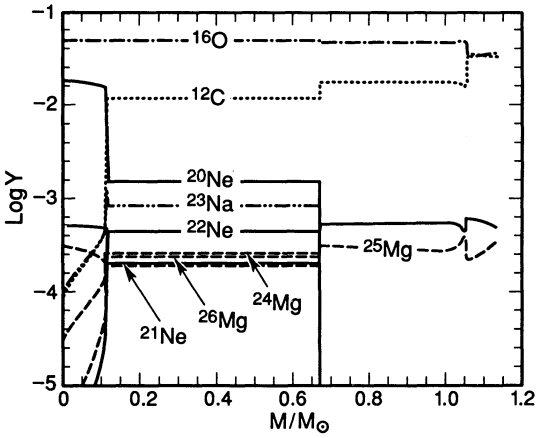

FIG. 14.—Abundances by number as a function of mass in the same model described in Fig. 12.

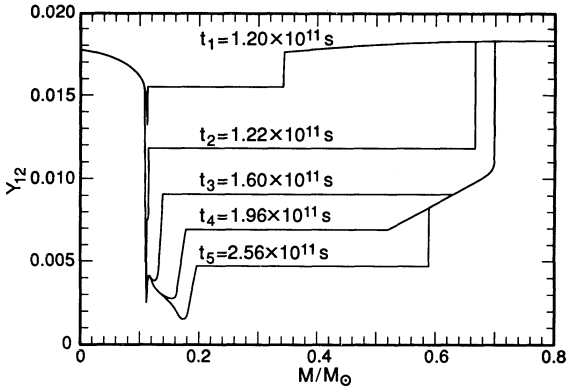

FIG. 16.—The abundance by mass of ^{12}C as a function of the mass coordinate at several times during the first convective shell phase.

Y_{12}, the abundance by number of ^{12}C, are shown in Figure 16 at various times during the existence of the first convective shell; for each time, the location of the convective shell is identifiable as the region where the ^{12}C abundance is constant. There is a very sharp discontinuity in the ^{12}C abundance profile below the base of the convective shell. This discontinuity arises because the carbon-burning rate at the high temperatures near the base of the convective shell are much larger than the *average* burning rate within the convective shell; because of this, the rate at which carbon is consumed in the radiative region just below the base of the convective shell is larger than the average rate of consumption of carbon (per gram per second) in the shell. The region within which carbon is smaller than in the convective shell is very narrow because (1) the drop in temperature between the base of the convective shell and the nearly isothermal interior is quite steep and (2) the carbon-burning rate depends on the temperature to a very high power.

Evolution of convective regions is shown again in Figure 17, but with the dominant isotopic composition highlighted. Note that ^{23}Na as well as ^{24}Mg are important isotopes in the ONe core. Dependences on time of the various luminosities and of stellar radius are shown in Figure 18. From Figure 11*a*, it is seen that, after maintaining a nearly constant value for some time (log $\Delta t \sim 11.1 \rightarrow 11.3$), the carbon-burning luminosity declines and the mass of the convective shell concomitantly decreases (Fig. 11*c*). However, as the mass of the convective shell becomes smaller, the peak in the carbon-burning rate shifts inward in mass to where there is more fuel.

As the first convective shell disappears, a new, but much milder, carbon flash occurs, giving rise to the formation of a second convective shell which, in contrast with the first convective shell, grows inward as well as outward in mass over most of its lifetime. Several more mild carbon flashes occur, accompanied by changes in the boundaries of convective regions. Each time, a flash occurs, the base of the convective region reaches nearer the center. Eventually, approximately 3×10^{11} s $\sim 10^4$ yr after the start of carbon-burning, ^{12}C is exhausted over a finite region about the center.

The evolution of the model center in the temperature-density plane is given in Figure 19. Labels along the curve mark positions for which some aspects of model evolution or composition has been provided in other figures: (1) $\Delta t = 1.0899913 \times 10^{11}$, just before the formation of the first convective shell which is driven by carbon burning (Figs. 8–10); (2) $\Delta t = 1.2270869 \times 10^{11}$, when the mass of the first convective shell is at a maximum (Figs. 12–15); and (3) $\Delta t = 3.4608966 \times 10^{11}$, after carbon has been exhausted at the center, just before the formation of a final convective shell due

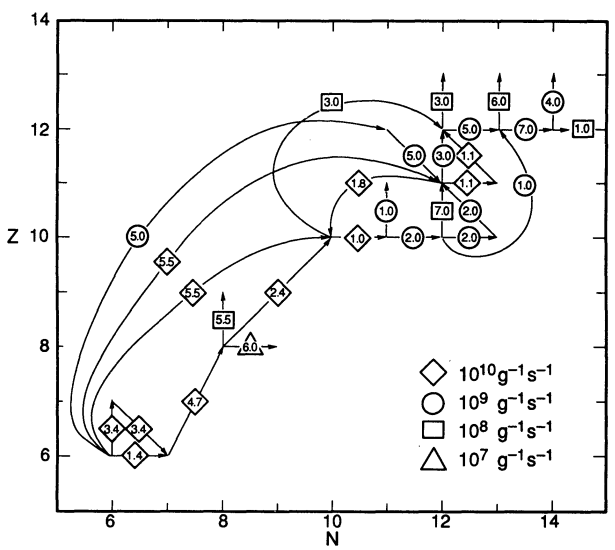

FIG. 15.—Reaction channels in the convective shell of the model described in Fig. 12. Rates are given in units of reactions g^{-1} s^{-1} times a power of 10: 10^{10} (*diamond*), 10^9 (*circle*), 10^8 (*square*), and 10^7 (*triangle*).

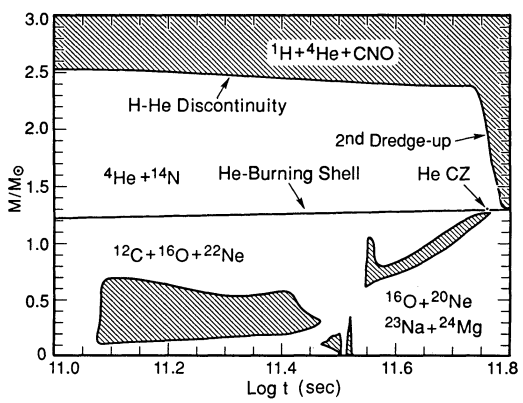

FIG. 17.—Time evolution of convective zones and composition during the carbon-burning phase. A convective zone formed above the base of the helium-burning shell during a mild helium shell flash is labeled "HeCZ".

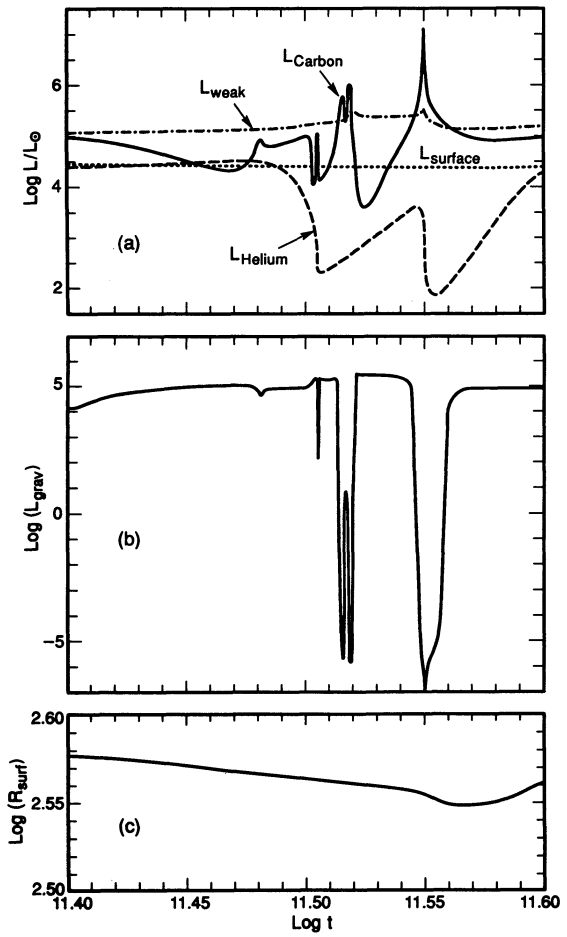

FIG. 18.—The time evolution of pertinent luminosities and stellar radius concentrating on the time when carbon is finally exhausted at the center. In panel (*a*) are surface luminosity $L_{\rm Surface}$, helium-burning luminosity $L_{\rm Helium}$, carbon-burning luminosity $L_{\rm Carbon}$, and the neutrino luminosity $L_{\rm neutrino}$. The rate of "gravitational" energy generation $L_{\rm grav}$ is in panel (*b*), and the surface radius is in panel (*c*).

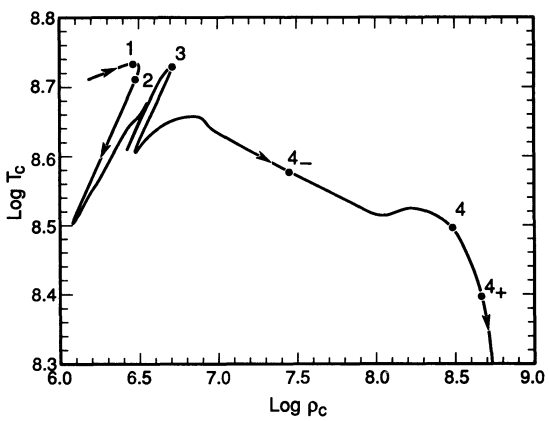

FIG. 19.—Evolution of the center of the model in the temperature-density plane. Labels along the curve mark positions for which some model information has been provided in other figures: (1) just before the formation of the first convective shell which is driven by carbon burning (Figs. 8–10); (2) when the mass of the first convective shell is at a maximum (Figs. 12–14); (3) after carbon has been exhausted at the center, just before the formation of a second convective shell due to carbon burning (Figs. 21–22); and (4) during the second dredge-up phase (Figs. 24–25). At points (4_-) and (4_+), composition profiles are given in Figs. 26 and 27, respectively.

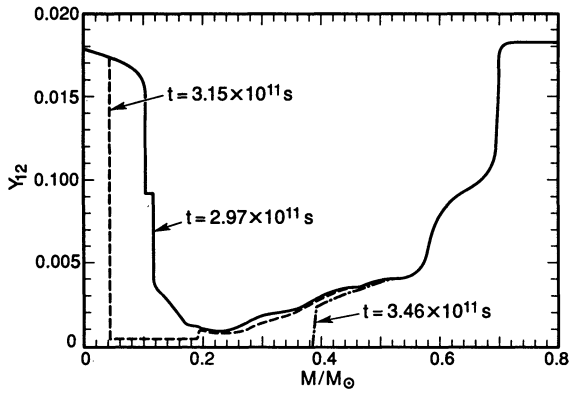

FIG. 20.—The abundance by mass of ^{12}C as a function of the mass coordinate during the period when the base of the carbon-burning region moves toward the center (times $\Delta t = 2.97 \times 10^{11}$ s and $= 3.15 \times 10^{11}$ s) and at a time when carbon has been effectively exhausted at the center and over a large region about the center ($\Delta t = 3.46 \times 10^{11}$ s).

to carbon burning (Figs. 21–22). The first large drop in temperature and density (following point [1]) occurs during the relaxation phase after the first carbon shell flash (see Fig. 7). The second drop occurs after convection has reached the center (at log $\Delta t \sim 11.52$), and the third occurs (after point [3]) in consequence of the large carbon flash which causes the formation of a final convective shell.

In Figure 20 are shown profiles of Y_{12} at two times during the existence of the second convective shell ($\Delta t = 2.97 \times 10^{11}$ s and $\Delta t = 3.15 \times 10^{11}$ s) and after carbon has effectively vanished from the center, just before the formation of a final convective shell driven by a carbon flash ($\Delta t = 3.46 \times 10^{11}$ s). Because there is a very sharp discontinuity in the energy generation rate at the boundary between the base of the convective shell and the radiative zone below it, causing the luminosity profile to resemble a step function, the calculation of models during times when the base of the convective shell is moving inward in mass requires a particular trick: for each new time step, the luminosity profile in the first trial model is chosen to be that in the previous converged model, but shifted inward by an amount dictated by the rate at which the base of the shell has been moving inward in previous models.

Abundances by mass of the major constituents in the model at time $\Delta t = 5.4288 \times 10^{11}$ s are shown in Figure 21 and abundances by number of other isotopes are shown in Figure 22.

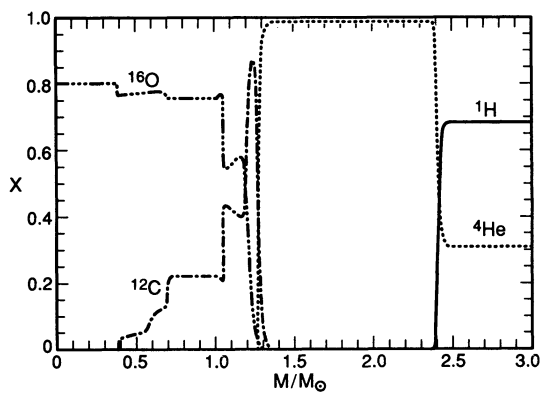

FIG. 21.—Abundances by mass when $\Delta t = 3.4608966 \times 10^{11}$ s (log $\Delta t = 11.539$), shortly after carbon has been exhausted over a large region about the center and just before a new convective shell forms.

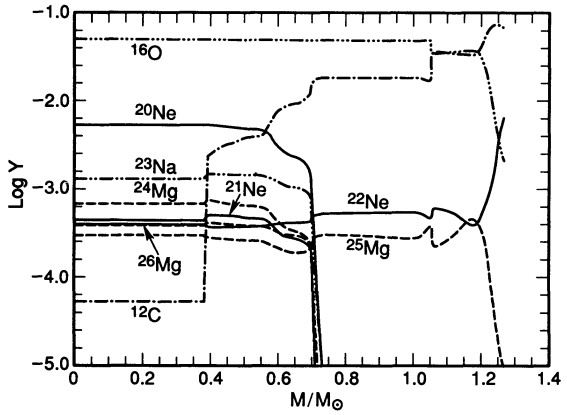

FIG. 22.—Number abundances of main isotopes as a function of mass in the helium-exhausted core of the same model described in Fig. 21.

Note that ^{23}Na is more abundant than ^{24}Mg in the inner 0.7 $M_\odot$ of the core. There are changes in the slopes of the abundance profiles at the mass coordinates $M/M_\odot \sim 0.6$ and $M/M_\odot \sim 0.7$. These mass coordinates correspond, respectively, to the location of the outer edge of the first convective shell when it is at the first and second relative maximum mass (see Figs. 11*c* and 17). The changes in slope at $M/M_\odot \sim 0.38$ mark the location of the outer edge of the carbon-exhausted core, which is at nearly the same mass as the outer edge of the last-formed convective zone which extends to the center.

4. FINAL DEVELOPMENT OF THE CARBON-EXHAUSTED CORE AND REDUCTION OF THE HYDROGEN-EXHAUSTED CORE BELOW THE CHANDRASEKHAR LIMIT

A carbon-burning runaway is already underway at time $\Delta t = 3.46 \times 10^{11}$ s ($\log \Delta t = 11.54$ in Figs. 11*a* and 18), and the associated large flux initiates the formation of a final convective shell (Fig. 11*c*). The initial base of this shell is at a mass of coordinate near $\sim 0.6\ M_\odot$, which coincides with the location of the outer edge of the first convective shell when it is at its second relative maximum in mass. The development of the final carbon flash is quite similar to that of the first flash (Fig. 11*a*). At the peak of the flash, $L_{\rm Carbon} \sim 1.5 \times 10^7\ L_\odot$ is approximately the same as at the peak of the first flash. After the relaxation phase following the flash, $L_{\rm Carbon}$ achieves a minimum value $\sim 10^5\ L_\odot$, similar to the minimum following the first flash.

Time dependences of various luminosities and of stellar radius during the final shell-burning phases are shown in Figure 23.

In contrast with the luminosity development after the first flash, $L_{\rm Carbon}$ steadily increases after the final flash, reaching a maximum value of $\sim 10^6\ L_\odot$ as the carbon-burning shell at the base of the associated convective shell approaches the helium-burning shell. The increase in luminosity is not due to the onset of another thermonuclear runaway. Instead, the increase is the normal response of a nuclear-burning shell above an electron-degenerate core to an increasing core mass. Over most of the interior of the carbon-exhausted core, $\epsilon_F/kT = 1$. As the carbon-exhausted core increases in mass, gravity exerts a stronger pull on matter above the core, leading to increasing pressures and temperatures and therefore to higher burning rates. The pressure of matter pushing outward at the base of the carbon-burning region is, to first order, balanced by the

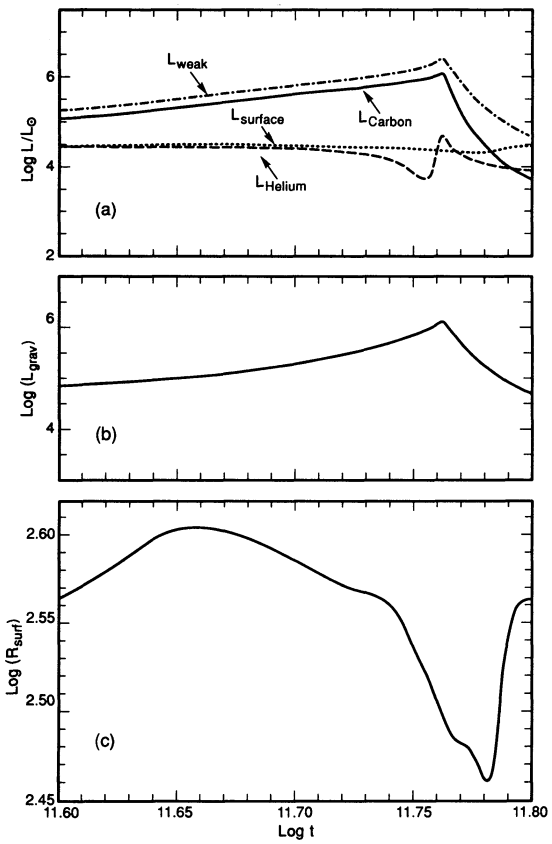

FIG. 23.—The time evolution of (*a*) the surface luminosity $L_{\rm Surface}$, helium-burning luminosity $L_{\rm Helium}$, carbon-burning luminosity $L_{\rm Carbon}$, and neutrino luminosity $L_{\rm neutrino}$; (*b*) the rate of "gravitational" energy generation $L_{\rm grav}$; and (*c*) the surface radius $R_{\rm surf}$ shortly before and during the completion of the second dredge-up phase.

weight of the matter between it and the helium-burning shell. When the mass of the intershell layer is reduced sufficiently in mass, pressures at the base of the carbon-burning shell decline and $L_{\rm Carbon}$ decreases. The high temperatures in the carbon-burning shell lead to a large neutrino luminosity, the energy for which comes from the release of gravitational potential energy by contracting matter below the burning shell and the release of internal thermal energy from the same region.

The "second dredge-up" phenomenon finally continues as $L_{\rm Carbon}$ approaches and recedes from its final major maximum. Luminosity and velocity characteristics of the model at time $\Delta t = 5.8835 \times 10^{11}$ s ($\log \Delta t = 11.77$), shortly after the final maximum in $L_{\rm Carbon}$ has been passed, are shown in Figure 24; rates of change of temperature and density are shown in Figure 25. At this time, the second dredge-up phase is about $\frac{3}{4}$ completed (Fig. 17) and the center of the model is located at point (4) in the temperature-density plane of Figure 19. The temperature at the base of the carbon-burning shell is almost 10^9 K, and the density there is about 5×10^5 g cm^{-3}, giving $\epsilon_F/kT \sim 8$. Figure 24*a* shows that most of the energy produced by nuclear burning ($L_{\rm Carbon} \sim 0.9 \times 10^6\ L_\odot$ and $L_{\rm Helium} \sim 3 \times 10^4\ L_\odot$) is absorbed by matter between the nuclear-burning region and the base of the convective envelope. As is evident from the velocity profile in Figure 24*b*, the absorbed energy pushes the absorbing matter outward.

The matter in the outwardly moving region is cooling (Fig. 25*a*) as it expands (Fig. 25*b*). It is worth demonstrating that the

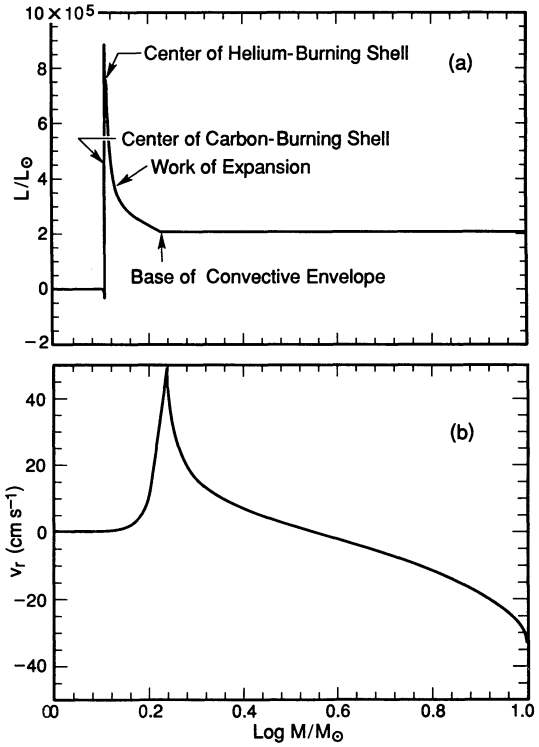

FIG. 24.—Mass dependence of (*a*) the luminosity and (*b*) matter velocity in the same model described in Fig. 23.

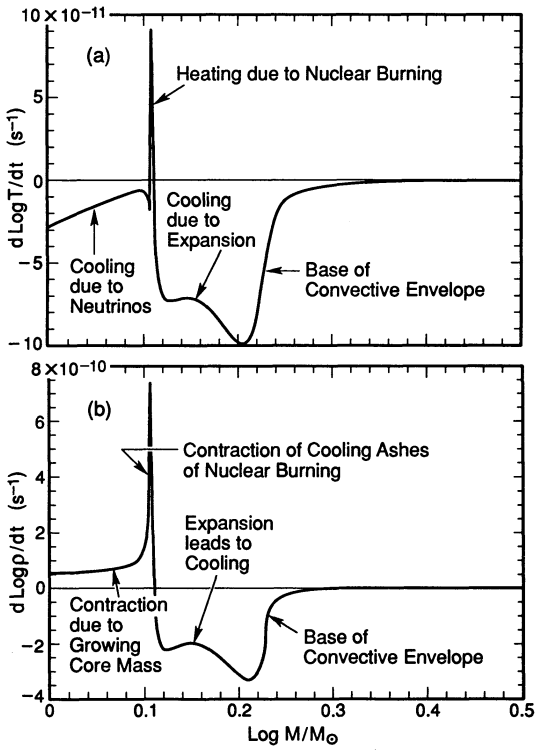

FIG. 25.—Mass dependence (*a*) of the rate of temperature increase and (*b*) of the rate of density increase when time $\Delta t = 5.8835 \times 10^{11}$ s ($\log \Delta = 11.7696$), during the second dredge-up episode.

time changes in thermodynamical properties at the base of the convective envelope, at the mass coordinate $\sim 1.7\ M_\odot$, imply that this base is moving inward in mass. At any point, the radiative gradient $V_{\rm rad} = (d \log T/d \log P)_{\rm rad}$ is proportional to $(P/T^4)\kappa L/M$, where P, T, κ, L, and M are the pressure, temperature, opacity, luminosity, and mass coordinate at that point. Figure 23*a* shows that $L = L_{\rm Surface}$ is decreasing. At the base of the convective envelope, the temperature ($\sim 10^6$ K) and density ($\sim 3 \times 10^{-5}$ g cm^{-3}) are such that electron scattering is the dominant source of opacity; hence, $\kappa \sim$ constant. If M is decreasing, then $V_{\rm rad}$ is certainly increasing if $P/T^4 (\propto \rho/T^3)$ is increasing. From Figures 25*a* and 25*b*, we see that, at the base of the convective envelope, the temperature is decreasing logarithmically at about half the rate at which density is decreasing logarithmically, so that $d \log (\rho/T^3)/dt \sim |d \log T/dt|$. Thus, the radiative gradient is increasing at the base. Since the adiabatic temperature gradient is essentially fixed at ~ 0.4, and since $V_{\rm rad}$ implies that matter is unstable against convection, it is clear that the base of the convective envelope must be moving inward in mass.

During the stalling phase, the rates of change $|d \log (\rho/dt)|$ and $|d \log T/dt|$ at the base of the convective envelope are ~ 50 times smaller than during the resumed second dredge-up phase (compare Figs. 10*a* and 10*b* with Figs. 25*a* and 25*b*). From Figures 10*a* and 10*b*, $d \log \rho/dt \sim 3 \times d \log T/dt$. Thus, during the stalling phase, $d \log (\rho/T^3)/dt \sim 0$ at a level nearly two orders of magnitude smaller than during the resumed second dredge-up phase, and the base of the convective envelope moves inward very slowly (Fig. 17).

Toward the end of the second dredge-up episode, the base of the convective envelope extends into the region where some helium has been converted into carbon. Although the surface abundances of the hydrogen-burning products ^{14}N and ^{4}He increase, the surface abundance of ^{12}C is not appreciably reduced; even though most of the additional ^{14}N was once ^{12}C, the destroyed ^{12}C has been replaced by ^{12}C made in the helium-burning region.

The abundances in the neighborhood of the helium-burning shell at a time somewhat before and at a time just after the dredge-up phase are shown in Figures 26 and 27, respectively. In the density-temperature plane of Figure 19, the models are at points (4_-) (Fig. 26) and (4_+) (Fig. 27). Note from Figure 17 that, at $\log \Delta t \sim 11.76$, a small convective zone appears, extending outward from the helium-burning shell and carrying outwards fresh ^{12}C and other products of helium burning. This

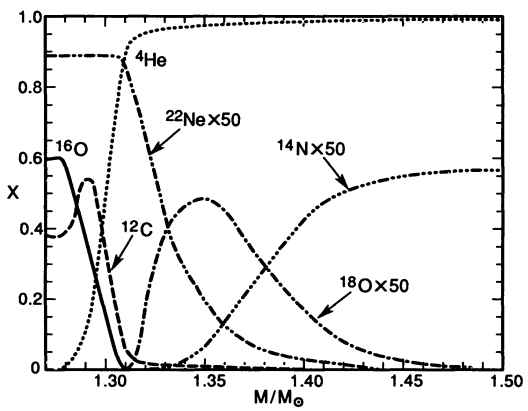

FIG. 26.—Composition near the start of the second dredge-up phase when $\Delta t = 5.4288 \times 10^{11}$ s ($\log \Delta t = 11.735$).

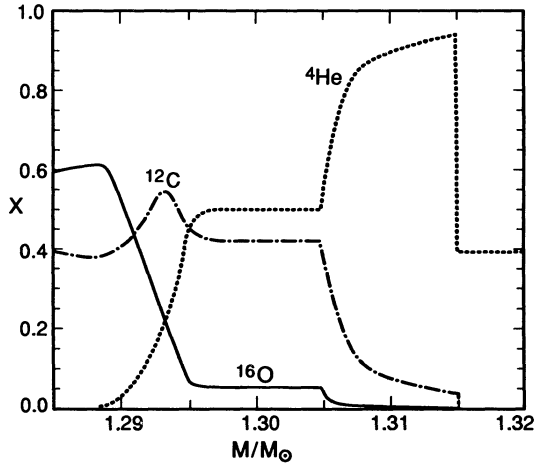

FIG. 27.—Composition at a time $\Delta t = 6.5291 \times 10^{11}$ s (log $\Delta t = 11.815$), somewhat after the second dredge-up phase has been completed.

zone is due to the occurrence of a mild helium shell flash (Figs. 11*a* and 11*c*). Convective mixing in this zone is responsible for the flat abundance profiles in Figure 27 between $M = 1.295\ M_\odot$ and $M = 1.305\ M_\odot$.

The radius of the model decreases noticeably during the second dredge-up episode (Fig. 23*c*). This is due to the decrease in pressure at given density and temperature occasioned by an increase in the mean molecular weight in the envelope as helium and heavier elements are dredged up.

At the end of the dredge-up episode, surface abundances are $X(^1\mathrm{H}) = 0.596$, $X(^3\mathrm{He}) = 1.04 \times 10^{-5}$, $X(^4\mathrm{He}) = 0.391$, $X(^{12}\mathrm{C}) = 0.00166$, $X(^{14}\mathrm{N}) = 0.00391$, $X(^{16}\mathrm{O}) = 0.00673$, $X(^{18}\mathrm{O}) = 7.72 \times 10^{-5}$, $X(^{22}\mathrm{Ne}) = 1.03 \times 10^{-4}$, and $X(^{25}\mathrm{Mg}) = 6.31 \times 10^{-9}$. The surface abundance of $^{13}\mathrm{C}$ is not appreciably altered.

Abundances of the most abundant isotopes in the interior of the last model are shown in Figure 28. The abundance of $^{23}\mathrm{Na}$ is an order of magnitude larger than has been assumed in the past in models of ONeMg white dwarfs. This means that, in models which produce an ONeMg core of mass near the Chandrasekhar mass, electron captures on $^{23}\mathrm{Na}$ rather than on $^{24}\mathrm{Mg}$ will initiate core collapse. It is now appropriate to call these cores ONeNa cores.

The abundances at the surfaces of two SAGB candidates. Antares and Betelgeuse, may be the consequence of the first and second dredge-up episodes, but the correspondence

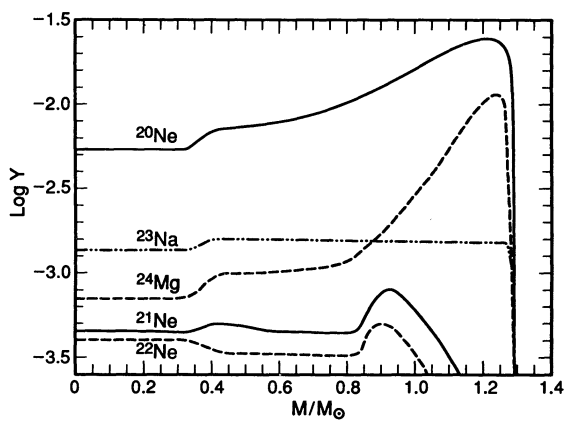

FIG. 28.—Composition in the carbon-exhausted interior of the last model.

between the model abundances and the stellar abundances is only qualitative. Lambert et al. (1984) find the CNO abundances at the surface of Betelgeuse to be in the ratios $X(^{12}\mathrm{C}):X(^{14}\mathrm{N}):X(^{16}\mathrm{O}) = 0.00146:0.00418:0.00458$. They find further that $^{12}\mathrm{C}/^{13}\mathrm{C} = 6 \pm 1$. At the surface of Antares, $^{12}\mathrm{C}/^{13}\mathrm{C} = 12 \pm 3$ (Harris & Lambert 1984). The qualitative concordance between theory and observation is that, in both cases, $^{12}\mathrm{C}/^{13}\mathrm{C}$ is substantially smaller than in the interstellar medium and, in the case of Betelgeuse, nitrogen is significantly more abundant than carbon. In order to match the stellar $^{12}\mathrm{C}/^{13}\mathrm{C}$ ratios quantitatively, we would need to assume either (1) that the initial ratio of $^{12}\mathrm{C}$ to $^{13}\mathrm{C}$ for Betelgeuse is ~ 8 and that for Antares is 25, or (2) that rotationally induced mixing during the main-sequence phase has mixed matter from the region of $^{13}\mathrm{C}$ production to the surface on a timescale shorter than the main-sequence lifetime.

5. SUMMARY AND CONCLUSIONS

We have calculated the evolution of a star of 10 $M_\odot$ and of Population I composition from the main sequence, through core helium burning, and through the early "super"-asymptotic giant branch; in the ESAGB phase, carbon is converted into oxygen and neon in a partially electron-degenerate core, shell helium burning is the dominant source of surface luminosity, and hydrogen does not burn. Two phases of dredge-up occur. The first occurs when the model evolves toward the giant branch after the exhaustion of hydrogen at the center; surface abundances are changed since the convective envelope extends into the region where freshly made $^{14}\mathrm{N}$, $^{13}\mathrm{C}$, $^4\mathrm{He}$, and $^3\mathrm{He}$ have been produced. The second dredge-up phase starts once core helium burning ceases and is due to an increasing opacity in the cooling and expanding region above the helium-burning shell. However, dredge-up is stalled by the onset of carbon burning, and the inner edge of the convective envelope remains just above the hydrogen-helium discontinuity.

Carbon burning starts off-center and propagates first outward and then inward. During both phases, the behaviors of the burning luminosity and the related convective zones are rather complicated. Strong carbon-burning runaways in a partially degenerate region alternate with almost stationary convective burning during the relaxation phase of the flashes. During most of the carbon-burning phase, the inner core of the star is effectively decoupled from the convective envelope, and an almost exact energy balance between neutrino losses, the energy released by carbon burning, and "gravitational energy" release is achieved. Nevertheless, the global structure of the star and the motion of the convective envelope are affected by the injection of carbon-burning energy. Ultimately, once carbon has been exhausted at the center, a strong carbon shell flash develops and propagates outward, leading to the exhaustion of carbon in the inner core. The second dredge-up process resumes during the relaxation phase of this final runaway. The inner edge of the convective envelope extends into the region where some helium has been converted into carbon and surface abundances are changed once again. The hydrogen-exhausted core then evolves into increasing degeneracy.

The observed surface abundances of two SAGB candidates (Antares and Betelgeuse) are in qualitative agreement with the results of our model calculations. We have not yet followed the thermally pulsing AGB phase and the interaction of the three burning shells (carbon, helium, and hydrogen) deserves further investigation.

The most abundant isotopes in the inert core are ^{16}O and ^{20}Ne, but, in contrast with previous studies, the abundance of ^{23}Na is almost 3 times larger than the abundance of ^{24}Mg and one order of magnitude larger than has been assumed in the past. Therefore, core collapse into a neutron star will be initiated by electron captures on ^{23}Na instead of on ^{24}Mg. Captures on ^{23}Na set in at modest densities and increase the electron molecular weight μ_e. Then, captures on ^{24}Mg increase μ_e still further. Next, captures on ^{20}Ne trigger O-Ne ignition and, ultimately, fast captures on the incinerated (nuclear statistical equilibrium) material induce gravitational collapse of the core (see Canal, Isern, & Labay 1992, Hashimoto, Iwamoto, & Nomoto 1993). Since μ_e is increased considerably by electron captures on ^{23}Na, and since captures on ^{20}Ne start at constant ρ/μ_e, we expect O-Ne ignition to occur at larger densities than currently estimated (Canal, Isern, & Labay 1992), thus opening new and interesting possibilities for the final fate of "ONeNa" cores near the Chandrasekhar mass. Work in this direction is underway.

The calculations on which this paper is based were done on computers at the National Center for Supercomputing Applications at the University of Illinois and at the Centre de Supercomputació de Catalunya under the project "Evolución Estelar con Pérdida de Masa" at the Universitat Politécnica de Catalunya in Barcelona. E. G.-B. thanks the Spanish Ministry of Education and Science for a Movilidad de Personal Investigador fellowship to do research at the University of Illinois where this project was initiated and I. I., Jr. thanks the Catalonian Ministry of Science and Education for funding a trip to Barcelona where the research was continued.

REFERENCES

Bao, Z. Y., & Käppeler, F. 1987, Atomic Data Nucl. Data Tables, 36, 411
Boothroyd, A. I., Sackmann, I.-J., & Ahern, S. C. 1993, ApJ, 416, 762
Caughlan, G. R., & Fowler, W. A. 1988, Atomic Data Nucl. Data Tables, 40, 283
Cameron, A. G. W. 1955, ApJ, 121, 144
Cameron, A. G. W., & Fowler, W. A. 1971, ApJ, 178, 433
Canal, R., Isern, J., & Labay, J. 1992, ApJ, 398, L49
Chen, K., & Leonard, P. J. T. 1993, ApJ, 411, L75
Dominguez, I., Tornambe, A., & Isern, J. 1993, ApJ, 419, 268
Fujimoto, M. Y., & Iben, I., Jr. 1992, 399, 646
Harris, M. J., & Lambert, D. L. 1984, ApJ, 281, 739
Hashimoto, M., Iwamoto, K., & Nomoto, K. 1993, ApJ, 414, L105
Hawkins, I., Craig, N., & Meyer, D. M. 1993, ApJ, 407, 185
Hoffleit, D., & Jaschele, C. 1982, The Bright Star Catalogue (New Haven: Yale Univ. Obs.)
Iben, I., Jr. 1964, ApJ, 140, 1631
———. 1965a, ApJ, 141, 993
———. 1965b, ApJ, 142, 1447
———. 1966, ApJ, 143, 483
———. 1975, ApJ, 196, 525
———. 1993, ApJ, 415, 767
Iben, I., Jr., Fujimoto, M. Y., & MacDonald, J. 1992, ApJ, 388, 521
Iben, I., Jr., & Renzini, A. 1983, ARA&A, 21, 271
Lambert, D. L., Brown, J. A., Hinkle, K. H., & Johnson, H. R. 1984, ApJ, 284, 223
Miyaji, S., & Nomoto, K. 1987, 318, 307
Miyaji, S., Nomoto, K., Yokoi, K., & Sugimoto, D. 1980, PASJ, 32, 303
Mustel, E. R., & Boyarchuk, M. E. 1959, Izv. Crimean Ap. Obs., 21, 3
———. 1960, Soviet Ast., 3, 744
Nomoto, K. 1984, ApJ, 277, 791
———. 1987, ApJ, 322, 206
Rogers, F. J., & Iglesias, C. A. 1992, ApJS, 79, 507
Sackmann, I.-J., & Boothroyd, A. I. 1992, ApJ, 392, L71
Sackmann, I.-J., Smith, R. L., & Despain, K. H. 1974, ApJ, 187, 555
Scalo, J. M., Despain, K. H., & Ulrich, R. K. 1975, ApJ, 196, 805
Smith, V. V., & Lambert, D. L. 1989, ApJ, 345, L75
———. 1990, ApJ, 361, L69
Smith, R. L., Sackmann, I.-J., & Despain, K. H. 1973, in Explosive Nucleosynthesis, ed. D. W. Schramm & W. D. Arnett (Austin: Univ. of Texas Press), 169
———. 1990
Sigurdsson, S., & Hernquist, L. 1992, ApJ, 401, L93
Snijders, M. A. J., Batt, T. J., Roche, P. F., Seaton, M. J. Morton, D. C., & Storey, P. J. 1987 MNRAS, 197, 107
Stothers, R. B., & Chin, C. 1993, ApJ, 412, 294
Truran, J. W. 1985, in Production and Distribution of CNO Elements, ed. J. Danziger, F. Matteucci, & K. Kjär (Garching: ESO), 211
———. 1990, in Physics of Classical Novae, ed. A. Cassatella & R. Viotti (Berlin: Springer), 373
Ulrich, R. K., & Scalo, J. M. 1972, ApJ, 176, L37
Williams, R. E. 1985, in Production and Distribution of CNO Elements, ed. J. Danziger, F. Matteucci, & K. Kjär (Garching: ESO), 225
Wood, P. R., Bessel, M. S., & Fox, M. W. 1983, ApJ, 272, 99